

Magnetic-field-induced superconductivity in hexalayer rhombohedral graphene

Jinghao Deng,¹ Jiabin Xie,¹ Hongyuan Li,¹ Takashi Taniguchi,²
Kenji Watanabe,³ Jie Shan,^{4,5} Kin Fai Mak,^{1,5} and Xiaomeng Liu^{1,*}

¹*Laboratory of Atomic and Solid State Physics, Cornell University, Ithaca, NY, USA*

²*Research Center for Materials Nanoarchitectonics,*

National Institute for Materials Science, 1-1 Namiki, Tsukuba 305-0044, Japan

³*Research Center for Electronic and Optical Materials,*

National Institute for Materials Science, 1-1 Namiki, Tsukuba 305-0044, Japan

⁴*School of Applied and Engineering Physics, Cornell University, Ithaca, NY, USA*

⁵*Max Planck Institute for the Structure and Dynamics of Matter, Hamburg, Germany*

In conventional superconductors, superconductivity is generally suppressed by external magnetic fields due to spin-singlet pairing. Here, we report signatures of in-plane-magnetic-field-induced superconductivity in hexalayer rhombohedral graphene and reveal electric-field control of its de-pairing behavior. With the application of a small in-plane magnetic field B_{\parallel} , a superconducting state emerges within a narrow band along a phase boundary. Its properties evolve continuously with increasing B_{\parallel} : the superconducting region progressively shifts toward higher electric field as the B_{\parallel} increases and the transition temperature rises with increasing B_{\parallel} . Remarkably, the superconducting state remains robust under B_{\parallel} up to 14 T, far exceeding the conventional Pauli limit. Quantum oscillation measurements further reveal that the superconductivity emerges from nematic Fermi surface reconstruction. These results suggest a spin-polarized superconducting states with unconventional origins.

Spin-polarized superconductivity has drawn significant interest due to its connection with spin-triplet pairing and unconventional order parameter [1–3]. In contrast to conventional Cooper pairs, spin-triplet superconductor bind electrons with identical spins and corresponds to an odd-parity order parameter, which may break time-reversal symmetry depending on its detailed structure. It may host exotic properties, such as Majorana zero modes, and could be relevant for topological quantum computing [4]. A common way to identify spin-polarized superconductivity is its resilience [2], or sometimes even reliance on magnetic fields [5–7]. Unlike conventional spin-singlet pairing, which is suppressed by the Zeeman effect of an external magnetic field, called the Pauli limit, spin-polarized superconductors do not incur a Zeeman energy penalty and can therefore remain stable under strong magnetic fields.

Rhombohedral multilayer graphene provides a clean platform for realizing and studying spin-polarized superconductivity with high reproducibility and tunability. Indications of spin-polarized superconductivity were first observed in a trilayer graphene system where the in-plane magnetic critical field is far beyond the Pauli limit [8]. Proximity-induced spin-orbit coupling and in-plane magnetic field can further stabilize and even promote the superconductivity in bilayer [9–11] and trilayer rhombohedral graphene [12, 13]. Pauli-limit violation behaviors in superconductivity in different parameter spaces are observed in thicker layer systems [14, 15], providing opportunities to investigate spin-triplet pairing and its interplay with different degrees of freedom, including isospin ordering, intervalley coherence, and Fermi surface reconstruction.

In this work, we report transport signatures of spin-polarized superconductivity induced by in-plane magnetic field in a hexalayer rhombohedral graphene system. The superconductivity can persist across a large range of electric and in-plane magnetic fields. We further uncover a close correlation between the electric field and magnetic-field range over which superconductivity emerges, which we attribute to orbital depairings effect arising from electric-field-controlled layer polarization. Quantum oscillation measurements identify the parent phase of the spin-polarized superconductivity as a nematic, partially isospin-polarized state. These results establish hexalayer rhombohedral graphene as a promising platform for exploring spin-polarized superconductivity.

Fig. 1(a) and (b) show the longitudinal resistance R_{xx} measured at in-plane magnetic field $B_{\parallel} = 0$ and 0.5 T at the base temperature of a dilution fridge (see Supplemental Materials [16] for experimental methods). Notably, we observe a butterfly-shaped phase boundary, marked by the dashed line in Fig. 1a, across which the resistance exhibits a sudden change (see Supplemental Materials [16] for calculations of n and E). This boundary likely indicates a Lifshitz transition—a change of the Fermi surface topology. Surprisingly, the application of small in-plane magnetic field $B_{\parallel} = 0.5$ T led to a resistance dip along low electric field regime of this phase boundary, suggesting a possible superconducting phase transition triggered by the in-plane magnetic field (Fig. 1(b)).

The in-plane-field-induced superconducting-like state clearly manifest in Fig. 1c. Line cuts of R_{xx} versus B_{\parallel} at zero electric field reveal a resistance dip that emerges above $B_{\parallel} \approx 0.07$ T and disappears beyond

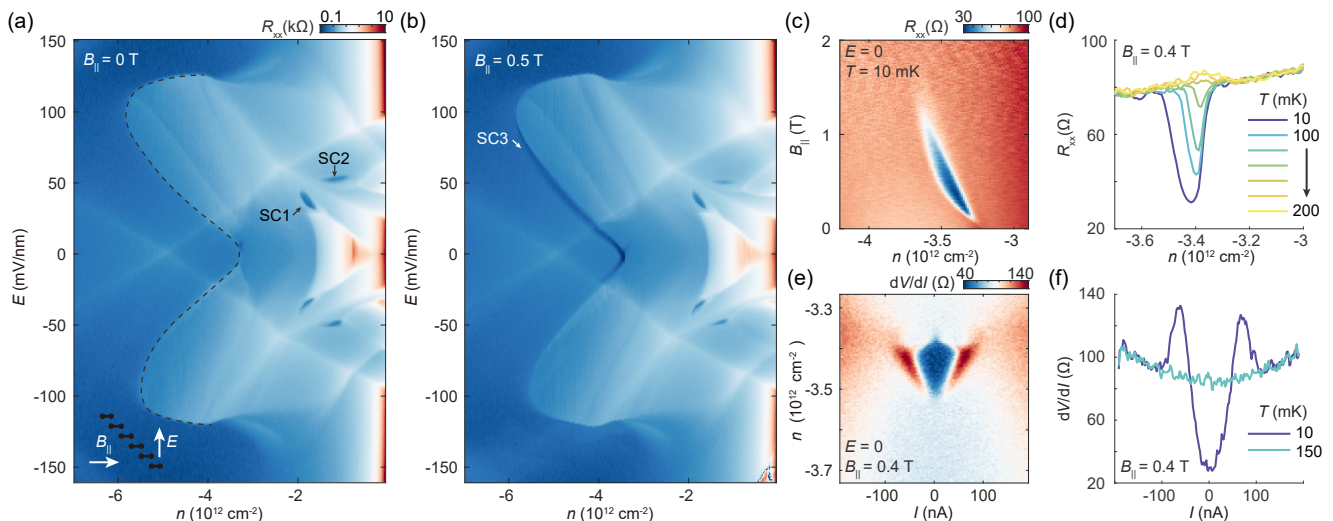


FIG. 1. In-plane-field-induced superconductivity in rhombohedral hexalayer graphene. (a),(b) Color-coded R_{xx} as a function of carrier density n and electric field E at zero field and at an in-plane magnetic field $B_{||} = 0.5$ T. The dashed curves indicate the phase boundary from which superconductivity arises. SC1 and SC2 correspond to previously reported superconducting states in this system [15]. SC3 denotes the superconducting phase observed in this work. The inset in panel (a) illustrates rhombohedral hexalayer graphene under electric field and inplane magnetic field. (c) $B_{||}$ -dependent R_{xx} - n line cuts at $E = 0$. At this specific electric field, superconductivity arises with $B_{||} \approx 0.07$ T and disappears above $B_{||} \approx 1.2$ T (d) Temperature dependence of R_{xx} vs n at $B_{||} = 0.4$ T. (e) Differential resistance dV/dI at $E = 0$ and $B_{||} = 0.4$ T. (f) dV/dI at $E = 0$, $B_{||} = 0.4$ T, and $n = -3.46 \times 10^{12} \text{ cm}^{-2}$, measured below and above the transition temperature at 10 mK and 150 mK, respectively.

$B_{||} \approx 1.2$ T. This in-plane-field response closely resembles the spin-polarized superconductivity previously reported in Bernal bilayer graphene [9].

With increasing $B_{||}$, the superconducting dip shifts toward higher hole densities (Fig. 1(c)), forming an arc, likely due to a Zeeman-effect-induced shift of the phase boundary between a spin-unpolarized metal on the left and a spin-polarized metal on the right. The superconducting feature appears closely connected to the Lifshitz transition: in Fig. 1(c), extrapolation of the superconducting arc toward zero $B_{||}$ intersects the step-like feature in the normal-state resistance.

Further evidence for this connection is provided by the temperature dependence at finite $B_{||}$. Fig. 1(d) shows density-dependent R_{xx} measured at $B_{||} = 0.4$ T and $E = 0$. As temperature increases, the resistance dip disappears, while the resistance peak associated with the transition between spin-polarized and spin-unpolarized states reappears on the higher-density side of the superconducting region. This behavior supports a direct connection between superconductivity and the Lifshitz transition above the critical temperature. The superconducting dip consistently occurs on the spin-unpolarized side of the phase boundary, suggesting that the in-plane magnetic field polarizes a nearby unpolarized state and stabilizes a superconducting ground state.

The superconducting character is further tested through I - V measurements. Figures 1(e) and 1(f)

present differential resistance dV/dI measured at $B_{||} = 0.4$ T and $E = 0$. Compared with $T = 150$ mK [Fig. 1(f)], dV/dI at base temperature exhibits pronounced nonlinear characteristics of a superconductor. The two peaks in dV/dI , corresponding to the superconducting critical current, reach their maximum near the Lifshitz-transition boundary and are suppressed toward both the spin-unpolarized and weakly polarized regimes.

Taken together, these measurements provide strong evidence for in-plane field induced superconductivity at a Lifshitz transition. We note that a finite residual resistance of approximately 37% of the normal-state value remains. Such residual resistance is commonly observed in rhombohedral graphene systems with low superconducting transition temperatures [17, 18].

To elucidate the evolution of superconductivity under an in-plane magnetic field, we measured a series of n - E - R_{xx} maps at various $B_{||}$ up to 14 T and summarize the resulting superconducting phase space in Fig. 2(a) (see Supplemental Material [16] for the complete dataset). Representative high-field R_{xx} maps at $B_{||} = 10$ T are shown in Figs. 2(b) and (c), taken below and above the superconducting transition temperature, respectively. Notably, increasing magnetic field suppresses superconductivity in the low- E region and causes the superconducting phase to shift toward higher electric fields. Strikingly, in the high E regime, superconductivity persists up to 14 T, the maximum field accessible in

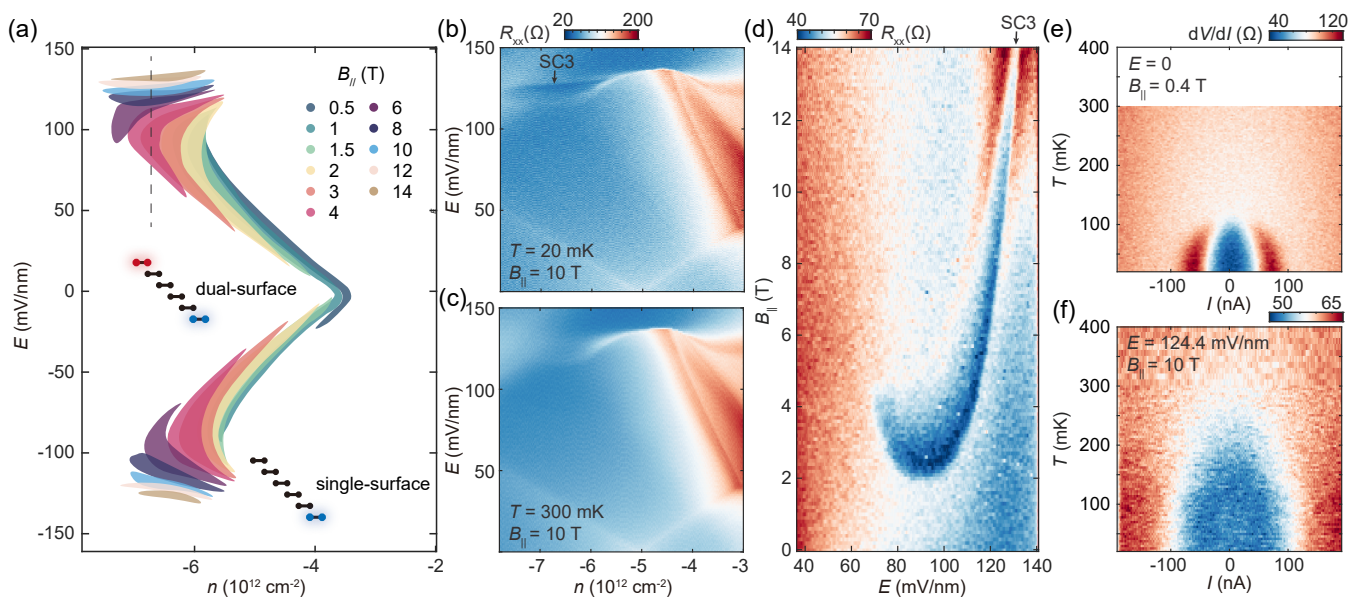


FIG. 2. Tunable superconductivity controlled by in-plane magnetic field and electric field. (a) Schematic of the superconducting phase space under various in-plane magnetic field, constructed from a series of n - E - R_{xx} maps (see Supplemental Material). The inset shows schematic wave-function weight distributions in rhombohedral hexalayer graphene at zero and large E , where red and blue indicate localization near the top and bottom surfaces, respectively. (b,c) n - E - R_{xx} maps measured at $(T, B_{\parallel}) = (20 \text{ mK}, 10 \text{ T})$ and $(300 \text{ mK}, 10 \text{ T})$, respectively. (d) R_{xx} vs E and B_{\parallel} measured at a fixed carrier density of $n = -6.57 \times 10^{12} \text{ cm}^{-2}$. The position of this linecut in n - E space is indicated by a vertical dashed line in (a). (e,f) Temperature-dependent differential resistance dV/dI measured at $B_{\parallel} = 0$ and $B_{\parallel} = 10 \text{ T}$, respectively. 0 T data is measured at $E = 0$, $n = -3.46 \times 10^{12} \text{ cm}^{-2}$, and 10 T data is measured at $E = 124.4 \text{ mV/nm}$ and $n = -6.57 \times 10^{12} \text{ cm}^{-2}$.

our experiment [Fig. 2(d)]. To the best of our knowledge, this value represents the highest in-plane critical magnetic field reported to date in rhombohedral multi-layer graphene systems.

Figures 2(e) and (f) present representative temperature-dependent dV/dI measurements performed at $(E, B_{\parallel}) = (0, 0.4 \text{ T})$ and $(124.4 \text{ mV/nm}, 10 \text{ T})$, respectively. Remarkably, the superconducting state at $B_{\parallel} = 10 \text{ T}$ exhibits an enhanced critical temperature of $T_c \approx 260 \text{ mK}$, compared with $T_c \approx 110 \text{ mK}$ at $B_{\parallel} = 0.4 \text{ T}$, together with a significantly increased critical current. A complete set of density-, electric-field-, and temperature-dependent dV/dI measurements is provided in the Supplemental Material [16]. These results demonstrate that neither strong electric fields nor large in-plane magnetic fields suppress superconductivity; instead, they enhance it.

For conventional BCS superconductors, the Zeeman effect polarizes electron spins, breaking spin-singlet Cooper pairs and suppressing superconductivity at the Pauli-limited $B_P = 1.86 \text{ T/K} \times T_c$. Using the critical temperature $T_c \approx 110 \text{ mK}$ measured at $B_{\parallel} = 0.4 \text{ T}$, the corresponding Pauli limit is approximately 0.2 T. At zero electric field, superconductivity survives up to a critical field of approximately 1.2 T, already exceeding the Pauli limit. Under large electric fields, superconductivity further persists up to 14 T with an enhanced critical tem-

perature, exceeding the Pauli limit by nearly two orders of magnitude. These observations indicate that the superconducting state is immune to Zeeman pair breaking and provide strong evidence for spin-triplet pairing.

The lower critical field observed at zero electric field can be understood in terms of orbital depairing. Beyond Zeeman pair breaking, disorder, Rashba spin-orbit coupling (SOC), and orbital effects are known to suppress superconductivity [17, 19, 20]. Disorder can strongly suppress non- s -wave superconductivity, but its effect is not expected to depend sensitively on electric field. The intrinsic SOC in rhombohedral graphene is negligibly small, suggesting that orbital depairing is the dominant mechanism limiting the critical field. In a two-dimensional superconductor with finite thickness, an in-plane magnetic field can penetrate through the sample edges and thread magnetic flux, leading to orbital depairing characterized by a critical field of order

$$B_{c\parallel}^{\text{orb}} \sim \frac{\Phi_0}{\xi d_{\text{eff}}},$$

where $\Phi_0 = h/2e$ is the superconducting flux quantum, ξ is the coherence length, and d_{eff} is the effective thickness [19].

In rhombohedral hexalayer graphene, the low-energy electronic states are strongly localized at the top and bottom layers, separated by approximately 1.7 nm. At

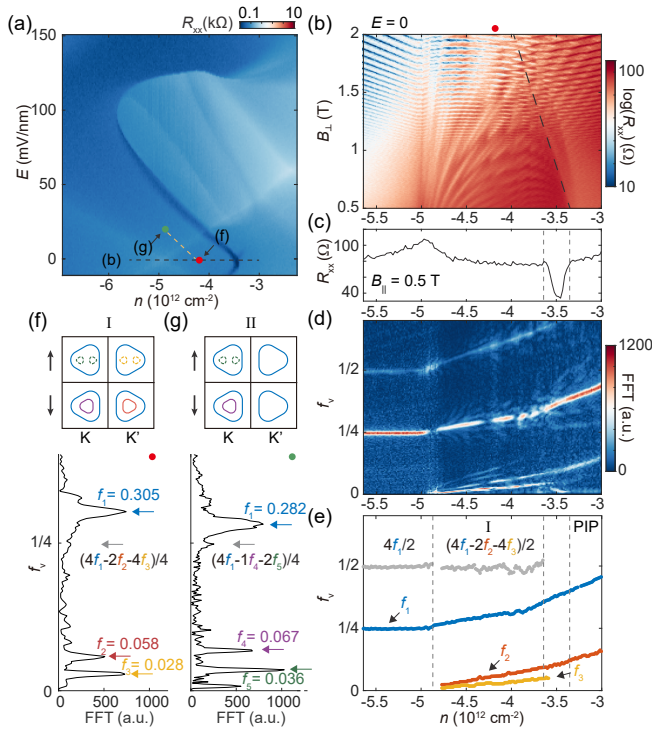


FIG. 3. Fermiology around the superconductivity. (a) R_{xx} - n - E map at $B_{\parallel} = 0.5$ T. The black and orange dashed lines indicate the SdH measurement paths corresponding to panels (b) and Fig. 4, respectively. The red and green dots mark the locations of the SdH measurements shown in panels (f) and (g). (b) R_{xx} as a function of carrier density n and out-of-plane magnetic field B_{\perp} . (c) R_{xx} versus carrier density n at $B_{\perp} = 0$ and in-plane magnetic field $B_{\parallel} = 0.5$ T, showing density range of superconductivity. (d), (e) FFT analysis of the quantum oscillations and the extracted peak frequencies at $E = 0$. Distinct peaks f_{ν} are indicated by colored markers in panel (e). The corresponding sum-rule results are shown as gray markers and are divided by 2 for clarity. (f), (g) Top panels show schematic Fermi-surface contours for representative phases corresponding to the red and green markers in panel (a). The labels I and II correspond to the same labels in panel (e) and Fig. 4(b). In each schematic, four pockets represent an approximate fourfold degeneracy arising from spin (\uparrow, \downarrow) and valley (K, K') degrees of freedom. Bottom panels show the FFT analysis of the quantum oscillations and the corresponding sum-rule calculations for the (n, E) positions indicated by the red and green dots in panel (a).

zero electric field, in the absence of correlation-induced polarization, the electronic states are symmetric superpositions of the top and bottom layers, susceptible of orbital depairing. Under large electric fields, however, the electronic wavefunctions become strongly polarized into the top or bottom layer. As a result, the effective thickness d_{eff} is significantly reduced, providing a natural explanation for the enhanced robustness of superconductivity. This electric-field-tunable orbital depairing suggests that the zero-field superconducting state involves contributions from both surfaces.

We next carry out a fermiology analysis, which indicates that superconductivity emerges from an isospin-polarized nematic state. Figure 3(b) shows the quantum oscillations under an out-of-plane magnetic field B_{\perp} at $E = 0$. A marked change in the oscillation pattern occurs across a phase boundary indicated by the dashed line. This boundary shifts with increasing magnetic field, similar to the phase-boundary shift observed under an in-plane magnetic field in Fig. 1(c). The superconducting states notably reside on the high hole-doping side of this phase boundary (Fig. 3c).

We perform fast Fourier transforms (FFT) of the quantum oscillations and normalize the resulting frequencies by the carrier density, yielding the normalized quantum oscillation frequency $f_{\nu} = \frac{e}{nh} f_{\text{FFT}}$, where f_{FFT} is the oscillation frequency of R_{xx} as a function of $1/B_{\perp}$, and e and h are the electron charge and Planck constant, respectively [5]. This normalized frequency, plotted in Fig. 3(d), represents the fraction of the Fermi-surface area associated with each peak relative to the total occupied Fermi-surface area.

On the high hole-doping side of the phase boundary, where superconductivity emerges, three prominent frequency peaks f_1 , f_2 , and f_3 can be identified, marked by blue, red, and orange line in Figs. 3(e). The sum of these frequencies should satisfy the sum rule $\sum s k f_{\nu} = 1$, where $s = \pm 1$ corresponds to hole-like and electron-like Fermi surfaces in the hole-doped regime, and k represents the degeneracy of the Fermi surface. For a spin- and valley-degenerate metallic state with an annular Fermi surface, we expect $4f_{\text{major}} - 4f_{\text{minor}} = 1$, where f_{major} and f_{minor} denote the outer and inner Fermi contours, respectively. Here we instead observe an unexpected sum rule $4f_1 - 2f_2 - 4f_3 = 1$ [Figs. 3(e) and 3(f)].

One possible Fermi-surface structure consistent with this sum rule is illustrated in Fig. 3(f). For two isospin flavors, the inner annular Fermi contour splits into two smaller contours that contribute to the frequency f_3 . The unsplit inner annular contour of the remaining two flavors corresponds to f_2 , together with a fourfold-degenerate outer Fermi contour corresponding to f_1 . Such splitting can be phenomenologically attributed to trigonal-warping effects near the band edge of rhombohedral multilayer graphene, in conjunction with nematicity that breaks the C_3 crystalline rotational symmetry [17, 21, 22].

At the low hole-doping side of the phase boundary, the FFT spectra exhibit two major frequency peaks, but no sum rule can be found. Such behavior is often found in iso-spin imbalanced states, where hole occupation in one spin band is greater than the other, also known as partial-isospin-polarized (PIP) state [23]. This state features a net spin polarization, which is consistent with shifting of the phase boundary under magnetic fields shown in Fig. 1(c) and 3(b).

At $|E| > 10$ mV/nm, we observe a different sum rule:

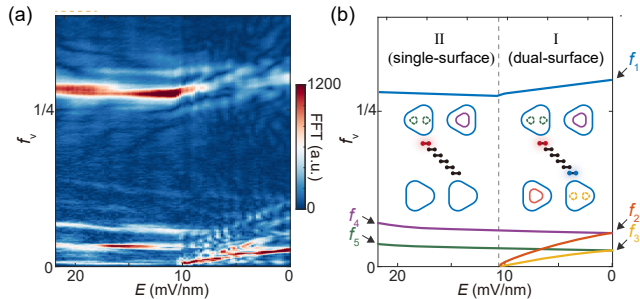


FIG. 4. Dual-surface to single-surface nematic Fermi surface transition. (a) Linecut of carrier-density-normalized FFT from R_{xx} as a function of $1/B_{\perp}$ along the orange dashed line in Fig. 3(a). (b) Sketch of the frequency peaks in (a). Inset shows schematic diagram of dual-surface and single-surface nematicity behavior in regions I and II, respectively

$4f_1 - f_4 - 2f_5 = 1$, as shown in Fig. 3(g) for measurements taken at the green dot in Fig. 3(a). Compared to the $E = 0$ case, the degeneracy of both the inner annular Fermi surface and the nematic Fermi pockets is reduced by a factor of two, suggesting the Fermi-surface configuration illustrated in Fig. 3(g).

The reduction of degeneracy is further captured in Fig. 4, which shows quantum oscillations measured along the path marked by the orange dashed line in Fig. 3(a). Under electric field, we observe that f_2 and f_3 split into two distinct branches: f_2 and f_3 ; f_4 and f_5 . As the electric field increases, f_2 and f_3 gradually decrease and eventually disappear for $E > 10$ mV/nm. This contrasting electric-field response suggests that the two branches originate from Fermi surfaces localized on the opposite graphene layers. At $E = 0$, electron states are evenly distributed between the top and bottom graphene layer. As the electric field increases, electrons become increasingly polarized toward one layer, while f_2 and f_3 associated with the opposite layer shrink and ultimately vanish, leaving only a single branch of the Fermi surfaces, f_4 and f_5 , for $E > 10$ mV/nm. This transition from a dual-surface nematic state to a single-surface nematic state is consistent with the observed electric-field modulation of orbital depairing.

In summary, our study reveals an in-plane-field-induced superconducting phase that survives under remarkably large in-plane magnetic fields. This suggests a spin-polarized superconducting state. The enhanced critical in-plane field at larger electric fields indicates a reduced effective thickness of the superconducting state due to layer polarization, which suppresses orbital depairing. Consistently, our fermiology analysis supports this layer-polarization transition and identifies nematic Fermi surface structures from which superconductivity emerges.

Note added.— During the preparation of this work, we became aware of several related studies reporting in-

plane-magnetic-field-induced or enhanced superconductivity [24–27].

ACKNOWLEDGMENTS

X. L. acknowledges support from the National Science Foundation through the CAREER program under Award No. DMR-2442363. J. D. acknowledges support from the New Frontier Grant, College of Arts & Sciences, Cornell University. The device fabrication is performed in part in Cornell Center for Materials Research and in part at the Cornell NanoScale Facility, a member of the National Nanotechnology Coordinated Infrastructure (NNCI), which is supported by the National Science Foundation (Grant NNCI-2025233). K.W. and T.T. acknowledge support from the JSPS KAKENHI (Grant Numbers 21H05233 and 23H02052), the CREST (JP-MJCR24A5), JST and World Premier International Research Center Initiative (WPI), MEXT, Japan.

* xl956@cornell.edu

- [1] S. Uji, H. Shinagawa, T. Terashima, T. Yakabe, Y. Terai, M. Tokumoto, A. Kobayashi, H. Tanaka, and H. Kobayashi, *Nature* **410**, 908 (2001).
- [2] S. Ran, C. Eckberg, Q.-P. Ding, Y. Furukawa, T. Metz, S. R. Saha, I.-L. Liu, M. Zic, H. Kim, J. Paglione, and N. P. Butch, *Science* **365**, 684 (2019).
- [3] L. Jiao, S. Howard, S. Ran, Z. Wang, J. O. Rodriguez, M. Sigrist, Z. Wang, N. P. Butch, and V. Madhavan, *Nature* **579**, 523 (2020).
- [4] M. Sato and Y. Ando, *Reports on Progress in Physics* **80**, 076501 (2017).
- [5] D. Shoenberg, *Magnetic Oscillations in Metals*, Cambridge Monographs on Physics (Cambridge University Press, Cambridge, 1984).
- [6] T. Konoike, S. Uji, T. Terashima, M. Nishimura, S. Yasuzuka, K. Enomoto, H. Fujiwara, B. Zhang, and H. Kobayashi, *Physical Review B* **70**, 094514 (2004).
- [7] S. Ran, I.-L. Liu, Y. S. Eo, D. J. Campbell, P. M. Neves, W. T. Fuhrman, S. R. Saha, C. Eckberg, H. Kim, D. Graf, F. Balakirev, J. Singleton, J. Paglione, and N. P. Butch, *Nature Physics* **15**, 1250 (2019).
- [8] H. Zhou, T. Xie, T. Taniguchi, K. Watanabe, and A. F. Young, *Nature* **598**, 434 (2021).
- [9] H. Zhou, L. Holleis, Y. Saito, L. Cohen, W. Huynh, C. L. Patterson, F. Yang, T. Taniguchi, K. Watanabe, and A. F. Young, *Science* **375**, 774 (2022).
- [10] C. Li, F. Xu, B. Li, J. Li, G. Li, K. Watanabe, T. Taniguchi, B. Tong, J. Shen, L. Lu, J. Jia, F. Wu, X. Liu, and T. Li, *Nature* **631**, 300 (2024).
- [11] Y. Zhang, G. Shavit, H. Ma, Y. Han, C. W. Siu, A. Mukherjee, K. Watanabe, T. Taniguchi, D. Hsieh, C. Lewandowski, F. von Oppen, Y. Oreg, and S. Nadj-Perge, *Nature* **641**, 625 (2025).
- [12] C. L. Patterson, O. I. Sheekey, T. B. Arp, L. F. W. Holleis, J. M. Koh, Y. Choi, T. Xie, S. Xu, Y. Guo, H. Stoyanov, E. Redekop, C. Zhang, G. Babikyan,

- D. Gong, H. Zhou, X. Cheng, T. Taniguchi, K. Watanabe, M. E. Huber, C. Jin, É. Lantagne-Hurtubise, J. Alicea, and A. F. Young, *Nature* **641**, 632 (2025).
- [13] J. Yang, X. Shi, S. Ye, C. Yoon, Z. Lu, V. Kakani, T. Han, J. Seo, L. Shi, K. Watanabe, T. Taniguchi, F. Zhang, and L. Ju, *Nature Materials* **24**, 1058 (2025).
- [14] T. Han, Z. Lu, Z. Hadjri, L. Shi, Z. Wu, W. Xu, Y. Yao, A. A. Cotten, O. Sharifi Sedeh, H. Weldeyesus, J. Yang, J. Seo, S. Ye, M. Zhou, H. Liu, G. Shi, Z. Hua, K. Watanabe, T. Taniguchi, P. Xiong, D. M. Zumbühl, L. Fu, and L. Ju, *Nature* **643**, 654 (2025).
- [15] J. Deng, J. Xie, H. Li, T. Taniguchi, K. Watanabe, J. Shan, K. F. Mak, and X. Liu, Superconductivity and ferroelectric orbital magnetism in semimetallic rhombohedral hexalayer graphene (2025), arXiv:2508.15909 [cond-mat].
- [16] See Supplemental Materials for additional experimental data, analysis, and Methods.
- [17] L. Holleis, C. L. Patterson, Y. Zhang, Y. Vituri, H. M. Yoo, H. Zhou, T. Taniguchi, K. Watanabe, E. Berg, S. Nadj-Perge, and A. F. Young, *Nature Physics* **21**, 444 (2025).
- [18] M. Kumar, D. Waleffe, A. Okounkova, R. Tejani, V. T. Phong, K. Watanabe, T. Taniguchi, C. Lewandowski, J. Folk, and M. Yankowitz, Superconductivity from dual-surface carriers in rhombohedral graphene (2025), arXiv:2507.18598 [cond-mat].
- [19] M. Tinkham, *Introduction to Superconductivity* (Courier Corporation, 2004).
- [20] Y. Zhang, R. Polski, A. Thomson, É. Lantagne-Hurtubise, C. Lewandowski, H. Zhou, K. Watanabe, T. Taniguchi, J. Alicea, and S. Nadj-Perge, *Nature* **613**, 268 (2023).
- [21] C. Huang, T. M. R. Wolf, W. Qin, N. Wei, I. V. Blinov, and A. H. MacDonald, *Physical Review B* **107**, L121405 (2023).
- [22] M. Koshino and E. McCann, *Physical Review B* **80**, 165409 (2009).
- [23] H. Zhou, T. Xie, A. Ghazaryan, T. Holder, J. R. Ehrets, E. M. Spanton, T. Taniguchi, K. Watanabe, E. Berg, M. Serbyn, and A. F. Young, *Nature* **598**, 429 (2021).
- [24] M. Kumar, D. Waleffe, A. Okounkova, R. Tejani, K. Watanabe, T. Taniguchi, É. Lantagne-Hurtubise, J. Folk, and M. Yankowitz, Pervasive spin-triplet superconductivity in rhombohedral graphene (2025), arXiv:2511.16578 [cond-mat].
- [25] Y. Guo, O. I. Sheekey, T. Arp, K. Kolář, T. Charpentier, L. Holleis, B. Foutty, A. Keough, M. Kang-Chou, M. E. Huber, T. Taniguchi, K. Watanabe, C. Lewandowski, and A. F. Young, Flat band surface state superconductivity in thick rhombohedral graphene (2025), arXiv:2511.17423 [cond-mat].
- [26] J. Yang, O. S. Sedeh, C. Yoon, S. Ye, H. Weldeyesus, A. Cotten, T. Han, Z. Lu, Z. Hadjri, J. Seo, L. Shi, E. Aitken, P. P. Liang, Z. Wu, M. Xu, C. Scheller, M. Zheng, R. Gazizulin, K. Watanabe, T. Taniguchi, D. Laroche, M. Li, F. Zhang, D. M. Zumbühl, and L. Ju, Magnetic field-enhanced graphene superconductivity with record pauli-limit violation (2025), arXiv:2510.10873 [cond-mat].
- [27] J. Xie, Z. Huo, Z. Chen, Z. Zhang, K. Watanabe, T. Taniguchi, X. Lin, and X. Lu, Magnetic-field-driven insulator-superconductor transition in rhombohe-
- dral graphene (2025), arXiv:2512.24306 [cond-mat].

Supplemental Materials for:

**Magnetic-field-induced superconductivity in hexalayer
rhombohedral graphene**

Jinghao Deng¹, Jiabin Xie¹, Hongyuan Li¹, Takashi Taniguchi², Kenji Watanabe³, Jie

Shan^{4,5}, Kin Fai Mak^{1,5}, Xiaomeng Liu^{1}*

¹Laboratory of Atomic and Solid State Physics, Cornell University, Ithaca, NY, USA

²Research Center for Materials Nanoarchitectonics, National Institute for Materials Science, 1-1 Namiki, Tsukuba 305-0044, Japan

³Research Center for Electronic and Optical Materials, National Institute for Materials Science, 1-1 Namiki, Tsukuba 305-0044, Japan

⁴School of Applied and Engineering Physics, Cornell University, Ithaca, NY, USA

⁵Max Planck Institute for the Structure and Dynamics of Matter, Hamburg, Germany

**Correspondence author E-mail: xl956@cornell.edu*

Experimental Methods

Device preparations. Hexalayer graphene and hBN flakes were mechanically exfoliated from high-quality graphite and hBN single crystals onto SiO₂/Si substrates. We treated the substrate with oxygen-plasma to enhance the yield of rhombohedral graphene. Rhombohedral domains were identified at room temperature by Raman spectroscopy (532 nm) and isolated using anodic oxidation lithography with an atomic force microscope. We utilized a standard dry transfer technique to pick up heterostructures with a PC/PDMS stamp in the sequence graphite (top gate)/hBN/rhombohedral graphene/hBN/graphite (bottom gate) and released onto pre-patterned SiO₂/Si substrates. Hall bar devices were defined by CHF₃/O₂ and O₂ plasma etching. Electrical contacts to rhombohedral graphene layers were formed by depositing Cr (5 nm)/Pd (15 nm)/Au (80 nm) after a brief CHF₃/O₂ plasma etch.

Transport measurements. The devices were studied in an Oxford Proteox dilution refrigerator with a base temperature of 9 mK. Stanford SR860 lock-in amplifiers were used for DC transport measurements with the frequency ranging from 17.777 to 37.777 Hz, depending on the low-pass filter time constant. We measure longitudinal four-terminal voltages and bias current simultaneously to obtain R_{xx} . For current dependent dI/dI measurements, we use a Keithley 2450 with a 4.7 M Ω serial resistance to regulate DC current. We apply contact gate voltages $V_c = -95$ V to silicon for better electrical contact. We calculated carrier density and electric field by using formula $n = \epsilon_r \epsilon_0 (V_{TG}/d_{TG} + V_{BG}/d_{BG})/e$ and $E = (V_{TG}/d_{TG} - V_{BG}/d_{BG})/2$, where ϵ_r , ϵ_0 , V_{TG} , V_{BG} , d_{TG} , and d_{BG} correspond to relative dielectric constant, vacuum dielectric permission, top gate voltage, bottom gate voltage, top hBN thickness, back hBN thickness.

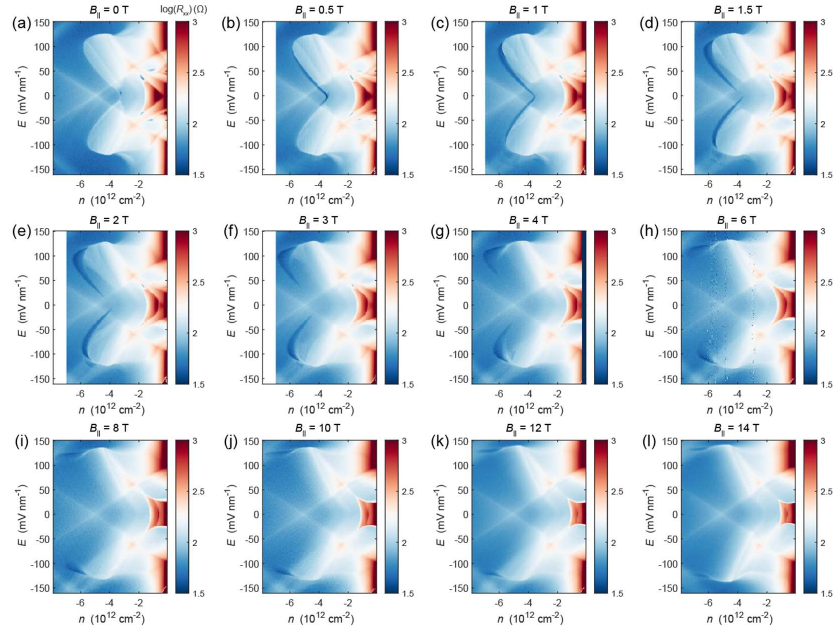


FIG. S1. In-plane magnetic field dependent n - E - R_{xx} maps from $B_{\parallel} = 0$ to 14 T. All resistance color scales are shown in logarithm scale for better visualization.

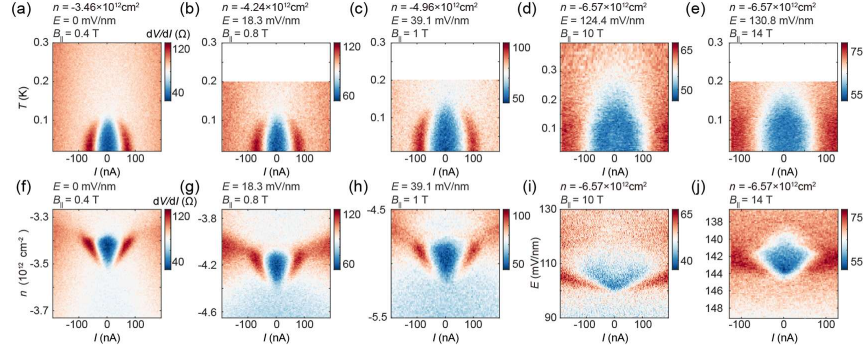


FIG. S2. Characterization the evolution of dV/dI spectra in different parameter spaces. (a) to (e) Temperature dependent differential resistance dV/dI measured at the superconducting states. (f) to (h) Carrier density dependent differential resistance evolution at fixed electric field. (i) and (j) Electric field dependent differential resistance evolution at fixed carrier density.